We are IntechOpen, the world's leading publisher of Open Access books Built by scientists, for scientists

6,900
Open access books available

185,000
International authors and editors

200M
Downloads

154
Countries delivered to

Our authors are among the

TOP 1%
most cited scientists

12.2%
Contributors from top 500 universities

CLARIVATE ANALYTICS
BOOK CITATION INDEX
INDEXED

WEB OF SCIENCE™

Selection of our books indexed in the Book Citation Index
in Web of Science™ Core Collection (BKCI)

Interested in publishing with us?
Contact book.department@intechopen.com

Numbers displayed above are based on latest data collected.
For more information visit www.intechopen.com

Carrier Dynamics and Magneto-Optical Properties of Cd$_{1\text{-}x}$Mn$_x$S Nanoparticles

Noelio Oliveira Dantas and Ernesto Soares de Freitas Neto

Additional information is available at the end of the chapter

1. Introduction

Cd$_{1\text{-}x}$Mn$_x$S nanoparticles (NPs) with size quantum confinement belong to the diluted magnetic semiconductor (DMS) quantum dot (QD) class of materials that has been widely studied in the last few years. The study of quasi-zero-dimensional Diluted Magnetic Semiconductors (DMS), such as Cd$_{1\text{-}x}$Mn$_x$S Quantum Dots (QDs), is strongly motivated due to the localization of magnetic ions in the same places as the free-like electron and hole carriers occurring in these nanomaterials [1,2]. This interesting phenomenon causes unique properties in DMS dots that can be explored in different technological applications, such as wavelength tunable lasers[3], solar cells[4,5], or in spintronic devices[6,7]. In this context, glass matrix-encapsulated Cd$_{1\text{-}x}$Mn$_x$S NPs emerge as potential candidates for several applications, given that this host transparent material is robust and provides excellent stability for DMS nanostructures. Therefore, the luminescent properties and carrier dynamics of Cd$_{1\text{-}x}$Mn$_x$S NPs should be comprehensively understood in order to target optical applications. For instance, different models based on rate equations can be employed to describe the temperature-dependent carrier dynamics of DMS nanostructures, such as they have been applied to semiconductor quantum wells[8], N-impurity complexes in III–V materials[9], and self-assembled semiconductor quantum dots[10].

It is well known that the optical properties of NPs can be significantly changed by interactions between nanostructures and their host material, due mainly to the formation of surface defects [11, 12]. These surface defects are heavily dependent on NP size and become more important with increasing surface–volume ratio. Generally, the comparison between the optical properties of Cd$_{1\text{-}x}$Mn$_x$S QDs and their corresponding bulk is obtained in different environments. To the best of our knowledge, this study is probably the first that simultaneously investigates both the carrier dynamics and the magneto-optical properties of Cd$_{1\text{-}x}$Mn$_x$S QDs and their corresponding bulk-like NC when both are embedded in the same host material.

Although the dot doped with impurities (metal and magnetic) are currently being synthesized by colloidal chemistry techniques [13,14], some possible applications require the nanoparticles (NPs) being embedded in robust and transparent host materials. In this context, the melting-nucleation approach appears as an appropriate synthesis technique since it allows the growth of DMS nanocrystals (NCs) embedded in different glass matrices. In addition to the controllable dot size and Mn^{2+} ion fraction incorporated into $Cd_{1-x}Mn_xS$ dots which can be achieved by this synthesis protocol, for example, the host glass matrix provides an excellent stability to the NPs. In particular for the melting-nucleation protocol used in this chapter, it is presented a discussion on the doping of QDs with magnetic impurities reasoned in two main models[3]: the 'trapped-dopant' and 'self-purification' mechanisms.

In this chapter, we have employed the optical absorption (OA), magnetic force microscopy (MFM), photoluminescence (PL), and magnetic circularly polarized photoluminescence (MCPL) measurements in order to investigate the properties of $Cd_{1-x}Mn_xS$ NPs that were successfully grown in a glass matrix. The organization of this chapter is shown as follows. In the section 2 (next section), we present the synthesis protocol that was employed in order to grow $Cd_{1-x}Mn_xS$ NPs in a glass matrix. The results obtained from the experimental techniques are presented and discussed in the section 3, highlighting the carrier dynamics and the magneto-optical properties of nanoparticles. We conclude our study in the section 4.

2. Synthesis of $Cd_{1-x}Mn_xS$ nanoparticles in a glass matrix

The host glass matrix for NP growth was labeled SNAB since its nominal composition is: $40SiO_2.30Na_2CO_3.1Al_2O_3.29B_2O_3$ (mol %). $Cd_{1-x}Mn_xS$ NPs were successfully synthesized in this glass matrix by adding 2[CdO + S] (wt % of SNAB), and x[Mn] (wt % of Cd), with x = 0.0, 0.5, 5.0, and 10 %. The synthesis method consists in a two sequential melting-nucleation approach, in which it is possible obtain ensembles of nearly spherical nanoparticles embedded in a glass matrix [12]. First, the powder mixture was melted in an alumina crucible at 1200 ºC for 30 minutes. Next, the melted mixture was quickly cooled down to room temperature where diffusion of Cd^{2+}, Mn^{2+}, and S^{2-} species took place. This diffusion resulted in $Cd_{1-x}Mn_xS$ NP growth in the SNAB glass environment.

In a second stage, a sample with x = 0.100 was subjected to a thermal annealing at 560 ºC for 6 h in order to enhance the diffusion of ions within the host SNAB matrix which promotes the growth of magnetic dots. Room temperature XRD pattern of the undoped CdS NPs (x = 0) embedded in the SNAB glass matrix was recorded with a XRD-6000 Shimadzu diffractometer using monochromatic Cu-$K_{\alpha 1}$ radiation (λ = 1.54056 Å). Thus, the wurtzite structure of CdS NPs embedded in the SNAB glass matrix has been confirmed. Evidently, the $Cd_{1-x}Mn_xS$ NPs with diluted magnetic doping have this same wurtzite structure, since it is a common phase for this DMS material.

3. Results and discussions

We have employed several experimental techniques in order to investigate the carrier dynamics and the magneto-optical properties of $Cd_{1-x}Mn_xS$ NPs. The room temperature

absorption band edge of synthesized Cd$_{1-x}$Mn$_x$S NCs was obtained with a double beam UV – VIS – NIR spectrophotometer (Varian, Cary 500) operating between 250 and 800 nm and with a spectral resolution of 1 nm. Photoluminescence (PL) measurements were taken with a 405 nm (~3.06 eV) continuous wave laser focused on a ~200 μm ray spot with an excitation power of 2.5 mW. Cd$_{1-x}$Mn$_x$S NP luminescence was collected using a USB4000 spectrometer from Ocean Optics equipped with a Toshiba TCD1304AP 3648-element linear CCD-array detector, in the 10 K to 300 K temperature range, with a 435 nm high-pass filter. The magnetic force microscopy images of the Cd$_{1-x}$Mn$_x$S NPs doped with x = 0.100 were recorded at room temperature with a scanning probe microscope (Shimadzu, SPM – 9600).

The magneto-photoluminescence (MPL) measurements were performed using superconductor coils (Oxford Instruments) with fields up to 15 T. The samples were placed into the liquid helium cryostat at 2 K and excited using a 405 nm (± 5 nm) continuous wave laser, from Laserline Laser Technology, focused on ~ 200 μm rays spot with excitation intensity values of 10 mW. The detected MPL was carried out with an ocean optics spectrometer (USB4000) and the polarization was analyzed using a $\lambda/4$ waveplate and with linear polarizer fixed parallel to the spectrometer entrance, in order to collect the photons with σ^+ and σ^- circular polarizations, respectively.

3.1. Carrier dynamics

The room temperature OA spectra of Cd$_{1-x}$Mn$_x$S NPs, with different x-concentrations, are shown in Fig. 1a. The formation of two well defined groups of Cd$_{1-x}$Mn$_x$S NPs of different sizes was confirmed by the two bands in the OA spectra. As indicated in Fig. 1a, these two groups of NPs were named: (i) QDs because their quantum confinement properties provoked a change in band energy around ~3 eV; and (ii) bulk-like NCs indicated by the absence of quantum confinement given the fixed band around ~2.58 eV, a value near the energy gap of bulk CdS [15,16]. At the bottom of Fig. 1a is the OA spectrum of the SNAB glass matrix where, in contrast, it can be seen that over a broad spectral range there is a complete absence of any band associated with NPs.

Figure 1a shows that the undoped CdS QDs (x = 0.000) exhibit confinement energy (E_{conf}) as indicated by the OA band peak at ~3.10 eV. From this value and using a confinement model based on effective mass approximation[12,15-18], the mean QD radius R was estimated by the expression: $E_{conf} = E_g + (\hbar^2\pi^2 / 2\mu R^2) - 1.8(e^2 / \varepsilon R)$, where E_g is the bulk material energy gap, μ is the reduced effective mass, e is the elementary charge, and ε is the dielectric constant. From this, a mean radius of about R~2.0 nm was estimated for the CdS QDs, thus confirming strong size quantum confinement [16].

Furthermore, the increase in x-concentration clearly induced a blue shift in the OA band of the Cd$_{1-x}$Mn$_x$S QDs from ~3.10 eV (x = 0.000) to ~3.22 eV for the highest magnetic doping (x = 0.100). Since these QDs were grown under identical synthesis conditions within the glass environment, it is expected that they would have the same mean size. As a result, there were no significant differences in the quantum confinements of these QDs that would cause shifts in the OA band peaks. Thus, it was concluded that the observed blue shift in OA band peak

(Fig. 1a) was a consequence of the **sp-d** exchange interactions between electrons confined in dot states and those located in the partially filled Mn^{2+} states. This explanation is reasonable since replacing Cd^{2+} with Mn^{2+} ions should increase the energy gap of $Cd_{1-x}Mn_xS$ QDs[18]. In addition, it is interesting to note the weak **sp-d** exchange interaction in the $Cd_{1-x}Mn_xS$ bulk-like NCs because their OA band remains in an almost fixed position (~2.58 eV).
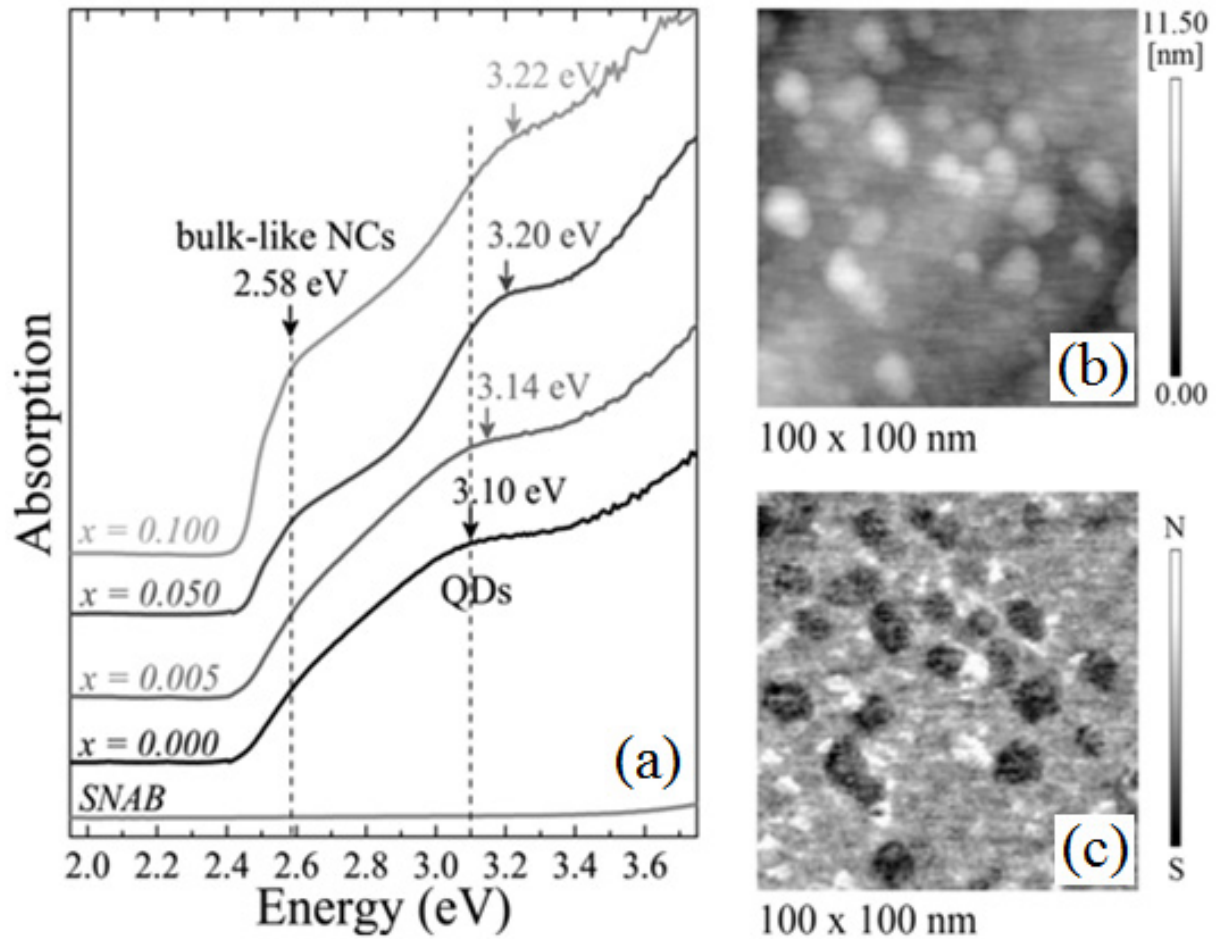

Figure 1. (a) Room temperature OA spectra of $Cd_{1-x}Mn_xS$ NPs with different x-concentrations embedded in the SNAB glass matrix. The two groups of NPs (QDs and bulk-like NCs) are indicated by the vertical dashed lines. The OA spectrum of the SNAB glass matrix is also shown at the bottom for comparison. (b) Topographic MFM image showing high quantities of $Cd_{0.900}Mn_{0.100}S$ NPs at the sample's surface, and (c) the corresponding phase MFM image (30 nm lift) where the contrast between the North (N) and South (S) magnetic poles identifies the orientation of the total magnetic moment of the DMS NPs.

Figure 1b presents the two-dimensional (100 x 100 nm) topographic MFM image of the sample with the highest level of magnetic doping (x = 0.100). Like the OA spectra, the topographic MFM image confirms the formation of two well defined groups of NPs with different mean radii: (i) R ~ 2.1 nm for the QDs, which closely agrees with the result estimated from the OA data (R ~ 2.0 nm); and (ii) R ~ 10.0 nm for the bulk-like NCs, a value near the vertical scale edge of Fig. 1b. Evidently, the exciton Bohr radius of bulk $Cd_{1-x}Mn_xS$ with diluted magnetic doping should be near that of bulk CdS, which is around a_B ~ 3.1 nm [16]. Hence, we can conclude that the QDs with mean radius R ~ 2.0 nm are under strong

quantum confinement, while the bulk-like NCs with mean radius R ~ 10.0 nm hardly exhibit any size confinement[19].

In addition, a large quantity $Cd_{1-x}Mn_xS$ NPs can be observed in Fig. 1b, as well as in the corresponding phase MFM image shown in Fig. 1c. These images reveal great proximity between the two groups of NPs (QDs and bulk-like NCs), so that strong coupling between their wave functions is expected. In Fig. 1c, the topographic signal can be neglected because its phase MFM was recorded with a 30 nm lift from the sample's surface. Thus, interaction between tip and NP magnetization induces the contrast observed in this phase MFM image. The dark area (light area) is caused by attraction (repulsion) between tip and NP magnetization represented by the South (North) magnetic pole in the vertical scale bar of Fig. 1c. Evidently, the magnetization in each NP (QD or bulk-like NC) is caused by the size-dependent **sp-d** exchange interactions, proving that Mn^{2+} ions are incorporated into the DMS nanostructures. This Mn^{2+} ion incorporation in NPs has also been established by electron paramagnetic resonance (EPR) measurements and simulations with other samples synthesized in the same way as in this research [17]. In Fig. 1c, it is interesting to note that there is a relationship between the NP size and the direction of its magnetic moment: small (large) NPs have their magnetic moment oriented towards the North (South) pole.

Figures 2a and b present, as examples, the effect of temperature on $Cd_{1-x}Mn_xS$ NP luminescence with x = 0.000 and 0.050. The emissions from the two groups of $Cd_{0.950}Mn_{0.050}S$ NPs with different sizes, QDs and bulk-like NCs, are clearly identified in Fig. 2b by the presence of two well defined PL bands which are in agreement with the OA spectra of Fig. 1. However, in Fig. 2a, a PL band can be observed whose complex nature is a result of the overlapping of several emissions, including those from deep defects: denominated as (1) and (2) for the QDs, as well as (1)[b] and (2)[b] for the bulk-like NCs. In a recent study of other similar $Cd_{1-x}Mn_xS$ NPs with wurtzite structure, the existence of emissions from two trap levels related to the presence of deep defects was demonstrated[20]. The origin of these defects in $Cd_{1-x}Mn_xS$ NPs (and CdS NPs) with hexagonal wurtzite structure is possibly related to two energetically different $V_{Cd} - V_S$ divacancies: one oriented along the hexagonal c-axis (assigned to trap (1)), and the other oriented along the basal Cd-S bond (assigned to trap (2))[20]. Furthermore, the size-dependence of these trap-levels, (1) and (2), has been confirmed for CdSe NCs [21], explaining the observed emissions from them in both the QDs (E_1 and E_2) and bulk-like NCs (E_1^b and E_2^b) that are embedded in our glass samples.

In Figs. 2a and b, all emissions are marked by vertical dotted lines, including the bound exciton emission (E_{exc}) of QDs as well as the electron-hole recombination (E_b) of bulk-like NCs. The characteristic emission of Mn^{2+} ions (E_{Mn}~2.12 eV) between the $^4T_1 - {}^6A_1$ levels in the $Cd_{1-x}Mn_xS$ NPs (with x ≠ 0) is also evident and represented in the Fig. 2c by $1/\tau_r^{Mn}$ rate [1,22,23]. The complete recombination aspects of these PL spectra are well-described in a diagram in Fig. 2c, where six (seven) emission bands can be identified for the CdS NPs ($Cd_{1-x}Mn_xS$ NPs with x ≠ 0). In Fig. 2b, the asymmetric shape of the emission band around 480 nm at low temperatures confirms the presence of shallow virtual levels for the QDs, and evidently there is also for the bulk-like NCs, as depicted in Fig. 2c. However, this emission

band (480 nm) becomes symmetric with rising temperature, which demonstrates that the trapped carriers in the virtual levels are being released to other non-radiative channels of QDs. It is interesting to note that in Fig. 2a the excitonic emission (E_{exc}) of CdS QDs is almost suppressed due to the strong presence of non-radiative channels, including one related to the energy transfer from QDs to bulk-like NCs. However, a comparison between the PL spectra of the CdS and the $Cd_{0.950}Mn_{0.050}S$ NPs (see Fig. 2) clearly reveals that increasing x-concentration induces gradual suppression of emissions from all trap-levels ((1), (2), (1)^b, and (2)^b), since Mn^{2+} ions are replacing the V_{Cd} vacancies in the NPs. Indeed, this fascinating behavior provides further evidence that the deep defects are caused by V_{Cd} –V_S divacancies, and that the NPs are actually being doped by Mn^{2+} ions. Hence, the non-radiative channels that supply the deep trap-levels disappear with increasing x-concentration in $Cd_{0.950}Mn_{0.050}S$ NPs, as shown in Fig. 2b.

In Fig. 2c, the wavy arrows represent non-radiative channels from the excitonic states of QDs, and from the conduction band (CB) of bulk-like NCs. Here, non-radiative energy transfer (ET) is given by the rate $1/\tau_{ET}^n$ (with n = A, B, C, A', and B'), where τ_{ET}^n is the carrier escape time from an NP to one of these five non-radiative transitions. In our model, we have assumed that the non-radiative paths from the excitonic states of QDs, as well as from the conduction band of bulk-like NCs to the deep trap-levels ((1), (2), (1)^b, and (2)^b) can be disregarded. However, it is evident that these deep trap-levels may be filled by carriers from: (i) the shallow virtual levels of QDs and bulk-like NCs; and (ii) the $^4T_1$ levels of Mn^{2+} ions[20]. Energy transfers from the excitonic states of QDs follow three paths: (A) to virtual levels (QDs); (B) to the conduction band of bulk-like NCs; and (C) to the $^4T_1$ level of Mn^{2+} ions. On the other hand, the energy transfers from the conduction band of bulk-like NCs follow two paths: (A') to virtual levels (bulk); and (B') to the $^4T_1$ level of Mn^{2+} ions. It is well known that the very fast energy transfer from a NP to Mn^{2+} ions is generally resonant due to the high density of states above the emissive $^4T_1$ level,[1] as shown by the $^{2,4}\Gamma$ levels in Fig. 2c. However, size quantum confinement can play an important role in this process that, besides being mediated by the **sp-d** exchange interactions, is strongly dependent on the Mn^{2+} fraction in $Cd_{1-x}Mn_xS$ NPs. In other words, QDs and bulk-like NCs are expected to behave differently due to the strong confinement of the QDs with a small mean radius of about R~2.0 nm.

The excitonic states of QDs can be denoted by $\left|1\right\rangle$, and the CB of bulk-like NCs by $\left|1^b\right\rangle$. The carrier number (depending on temperature T) of these two states is given by $N_1(T)$ and $N_1^b(T)$, respectively. Since carriers are thermally distributed each one of the three non-radiative channels related to QDs is supplied by $N_1(T)\exp(-E_n/K_BT)$ carriers, where E_n (with n = A, B, and C) is the corresponding activation energy of the non-radiative n channel. Similarly, $N_1^b(T)\exp(-E_n/K_BT)$ carriers are transferred to each one of the two non-radiative channels related to bulk-like NCs, where n = A', and B'. Furthermore, as shown in Fig. 2c by the straight, downward pointing arrows, radiative emissions are also present from both QDs and bulk-like NCs in the PL spectra which are related to $1/\tau_r^{QD}$ and $1/\tau_r^b$ rates, respectively. The straight, upward pointing arrow, indicated by g (g'), represents photo-excitation of the QDs (bulk-like NCs) caused by the laser pump. The carrier dynamics that take into account

these transitions from the $|1\rangle$ (QD) and $|1^b\rangle$ (bulk-like NC) levels can be described by the following rate equations:
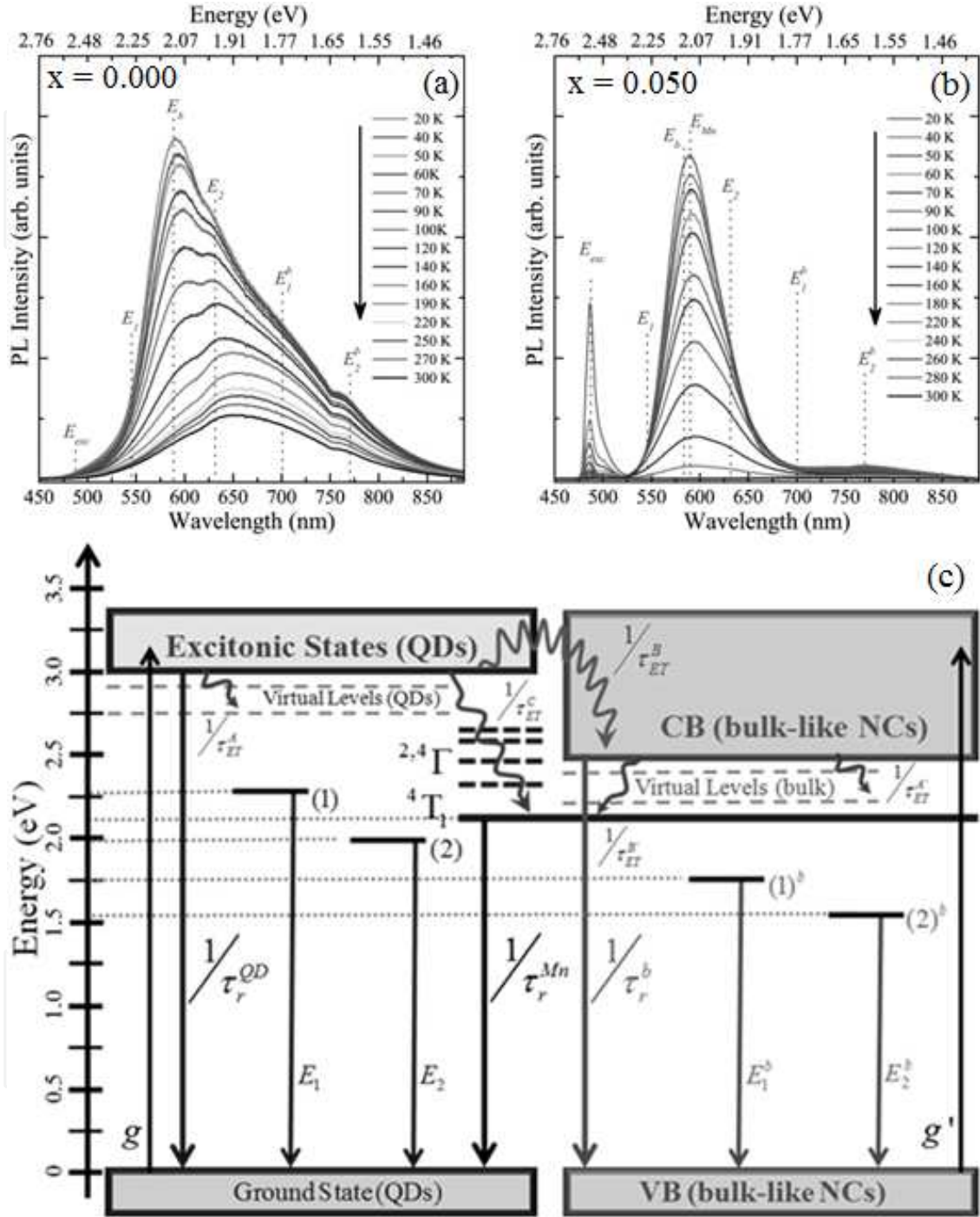

Figure 2. PL spectra of both (a) the CdS NPs (x = 0.000) and (b) Cd$_{0.950}$Mn$_{0.050}$S NPs at several temperatures, from 20 K (top) to 300 K (bottom), as indicated by the downward pointing arrows. Their recombination aspects are depicted in panel (c), where the emissions from both the QDs and the bulk-like NCs are clearly identified. In addition, the characteristic emission of Mn^{2+} ions (^{4}T$_1$–^{6}A$_1$), E$_{Mn}$ ~2.12 eV, when substitutionally incorporated in II-VI semiconductors is also evident. In the present energy scale, the ^{6}A$_1$ level of the Mn^{2+} ions is located at top of the QD ground state.

$$\frac{dN_1(T)}{dt} = +g - \underbrace{\frac{N_1(T)}{\tau_r^{QD}}}_{\substack{\text{radiative} \\ \text{emission}}} - \underbrace{\frac{N_1(T)\beta_A}{\tau_{ET}^A}}_{\text{QDs}\rightarrow\text{virtual levels (QDs)}} - \underbrace{\frac{N_1(T)\beta_B}{\tau_{ET}^B}}_{\text{QDs}\rightarrow\text{bulk-like NCs}} - \underbrace{\frac{N_1(T)\beta_C}{\tau_{ET}^C}}_{\text{QDs}\rightarrow Mn^{2+} \text{ ions}} \quad ; \tag{1}$$

$$\frac{dN_1^b(T)}{dt} = +g' + \underbrace{\frac{N_1(T)\beta_B}{\tau_{ET}^B}}_{\text{QDs}\rightarrow\text{bulk-like NCs}} - \underbrace{\frac{N_1^b(T)}{\tau_r^b}}_{\substack{\text{radiative} \\ \text{emission}}} - \underbrace{\frac{N_1^b(T)\beta_{A'}}{\tau_{ET}^{A'}}}_{\text{bulk-like NCs}\rightarrow\text{virtual levels (bulk)}} - \underbrace{\frac{N_1^b(T)\beta_{B'}}{\tau_{ET}^{B'}}}_{\text{bulk-like NCs}\rightarrow Mn^{2+} \text{ ions}} \quad ; \tag{2}$$

where $\beta_n = \exp(-E_n/K_B T)$ with n = A, B, C, A', and B'. In Eqs. (1) and (2), both the radiative emissions from QDs and bulk-like NCs and all non-radiative energy transfers are highlighted. In steady-state conditions, the laser excitations are given by $g = N_{1(0)}/\tau_r^{QD}$ and $g' = N_{1(0)}^b/\tau_r^b$ for QDs and bulk-like NCs, respectively. Moreover, there are no temporal changes in the carrier numbers, i.e., $\left(dN_1(T)/dt\right) = 0$ and $\left(dN_1^b(T)/dt\right) = 0$. When these conditions are replaced in Eqs. (1) and (2), we get:

$$N_1(T) = \frac{N_{1(0)}}{\left[1 + \alpha_A \exp\left(-E_A/K_B T\right) + \alpha_B \exp\left(-E_B/K_B T\right) + \alpha_C \exp\left(-E_C/K_B T\right)\right]} \quad ; \tag{3}$$

$$0 = +\frac{N_{1(0)}^b}{\tau_r^b} + N_1(T)\frac{\exp\left(-E_B/K_B T\right)}{\tau_{ET}^B} - N_1^b(T)\left[\frac{1}{\tau_r^b} + \frac{\exp\left(-E_{A'}/K_B T\right)}{\tau_{ET}^{A'}} + \frac{\exp\left(-E_{B'}/K_B T\right)}{\tau_{ET}^{B'}}\right] . \tag{4}$$

The carriers' number in the QDs ($|1\rangle$ level) as a function of temperature T is given by Eq. (3), where the term $\alpha_n = \left(\tau_r^{QD}/\tau_{ET}^n\right)$ (with n = A, B, and C) can be considered constant at first approximation. After replacing the term $N_1(T)$ (given by Eq. (3)) in Eq. (4), we get:

$$0 = +\frac{N_{1(0)}^b}{\tau_r^b} + \frac{N_{1(0)}}{\tau_{ET}^B\left[\exp\left(E_B/K_B T\right) + \alpha_A \exp\left[-(E_A - E_B)/K_B T\right] + \alpha_B + \alpha_C \exp\left[-(E_C - E_B)/K_B T\right]\right]} -$$
$$-N_1^b(T)\left[\frac{1}{\tau_r^b} + \frac{\exp\left(-E_{A'}/K_B T\right)}{\tau_{ET}^{A'}} + \frac{\exp\left(-E_{B'}/K_B T\right)}{\tau_{ET}^{B'}}\right] . \tag{5}$$

Evidently, the second term on the right side of Eq. (5) is related to the carrier-mediated energy transfer from QDs to bulk-like NCs, and can be defined by:

$$\frac{N_{1(0)}^b(T)}{\tau_r^b} = \frac{N_{1(0)}}{\tau_{ET}^B\left[\exp\left(E_B\Big/K_BT\right) + \alpha_A\exp\left[-\left(E_A - E_B\right)\Big/K_BT\right] + \alpha_B + \alpha_C\exp\left[-\left(E_C - E_B\right)\Big/K_BT\right]\right]} . \quad (6)$$

This represents temperature-dependent excitation of bulk-like NCs caused by carriers transferred from the QDs. Thus, Eq. (5) can be solved, resulting in the following expression:

$$N_1^b(T) = \frac{N_{1(0)}^b + N_{1(0)}^b(T)}{\left[1 + \alpha_{A'}\exp\left(\frac{-E_{A'}}{K_BT}\right) + \alpha_{B'}\exp\left(\frac{-E_{B'}}{K_BT}\right)\right]} , \quad (7)$$

where $\alpha_n = \left(\tau_r^b\Big/\tau_{ET}^n\right)$ with n = A', and B'. Eq. (7) describes the temperature dependence for the carrier number of the bulk-like NCs ($\left|1^b\right\rangle$ level), and the term $N_{1(0)}^b(T)$ is given by Eq. (6). From Eqs. (3) and (7), we can find the steady-state intensities $I^{QD}(T) = \left[N_1(T)\Big/\tau_r^{QD}\right]$ and $I^b(T) = \left[N_1^b(T)\Big/\tau_r^b\right]$ of the QDs and bulk-like NCs, respectively, which results in:

$$I^{QD}(T) = \frac{I_0^{QD}}{\left[1 + \alpha_A\exp\left(\frac{-E_A}{K_BT}\right) + \alpha_B\exp\left(\frac{-E_B}{K_BT}\right) + \alpha_C\exp\left(\frac{-E_C}{K_BT}\right)\right]} ; \quad (8)$$

$$I^b(T) = \frac{I_0^b(T)}{\left[1 + \alpha_{A'}\exp\left(\frac{-E_{A'}}{K_BT}\right) + \alpha_{B'}\exp\left(\frac{-E_{B'}}{K_BT}\right)\right]} . \quad (9)$$

In Eq. (8), it is interesting to note that the term $I_0^{QD} = \left[N_{1(0)}\Big/\tau_r^{QD}\right]$ is temperature-independent because it is only related to QD photo-absorption. On the other hand, in Eq. (9), the term $I_0^b(T) = \left\{\left[N_{1(0)}^b(T) + N_{1(0)}^b\right]\Big/\tau_r^b\right\}$ is temperature dependent and is given by Eq. (6) since the carrier-mediated energy transfer from QDs to bulk-like NCs is strongly temperature dependent. Evidently, there is coupling between Eqs. (8) and (9), and they can be fit to the experimental integrated PL intensity. This in turn, permits the deduction of activation energies related to the non-radiative channels of QDs (E_A, E_B, and E_C) as well as of bulk-like NCs ($E_{A'}$, and $E_{B'}$).

Figures 3a, b, and c show integrated PL intensity behavior for the doped Cd$_{1-x}$Mn$_x$S NPs (x ≠ 0) as a function of temperature. Here, the solid and open triangle symbols represent the bulk-like NCs and QDs, respectively. At low temperatures, QD emission intensity decreases quickly while bulk-like NC emissions remain almost constant except for a small increase at x = 0.100 (Fig. 3c). This behavior is due to the trapping of excited carriers from the excitonic states to the shallow virtual levels of QDs, where temperature increases induce a gradual

release of these carriers to other electronic states, including the CB of bulk-like NCs. This carrier-mediated energy transfer from QDs to bulk-like NCs is a tunnelling phenomenon that is strongly dependent on the coupling between the wave functions of these NPs[24]. This effect is expected, given the high proximity between QDs and bulk-like NCs as confirmed by the MFM images (Figs. 1b and c). The ratio between these PL peak intensities (bulk-like NCs/QDs) as a function of temperature is shown in the insets of Fig.3. Here, it can be seen that the ratio increases at low temperatures and then decreases as QD emissions remain constant and bulk-like NC emissions decrease.

In the insets of Fig. 3, a fitting procedure with a Gaussian-like component, gives the temperature that yields the maximum ratio for each x-concentration: 122 K (x = 0.005); 134 K (x = 0.050); and 127 K (x = 0.100). Moreover, the FWHM (Full Width at Half Maximum) of the Gaussian-like component broadens with increasing x-concentration: 63 K (x = 0.005); 70 K (x = 0.050); and 74 K (x = 0.100), thus confirming that emission intensity from bulk-like NCs decreases more slowly after the maximum ratio is reached. It is interesting to note that the peak ratio between the PL intensities of bulk-like NCs/QDs is related to the inflection point of the corresponding integrated PL intensity of bulk-like NCs. This is indicated by the dashed vertical lines in Figs. 3a, b, and c. The inflection point temperatures were attributed to the maximum thermal energy transfer process from QDs to bulk-like NCs.

It can be seen that the temperatures obtained by the Gaussian fitting (T = 122 K, 134 K, and 127 K) can be related to delocalization thermal energies (like K_BT)[25], which are needed to release the trapped carriers at shallow virtual levels (surface defects, for example) of QDs. Thus, the aforementioned E_A activation energy coupled to these virtual levels (QDs) could be found by using the following expression: $E_A = K_BT$; where K_B is the Boltzmann constant, and T is the temperature obtained by the Gaussian fitting. As a result, the x-concentration dependent behavior of this E_A activation energy is given by: 10.51 meV (x = 0.005); 11.54 meV (x = 0.050); and 10.94 meV (x = 0.100), where the deduced values remain almost invariable. This result can take into account two effects caused by the increasing x-concentration of $Cd_{1-x}Mn_xS$ QDs: (i) the increasing energy gap that was observed in OA spectra of Fig. 1a; and (ii) possible density amplification of virtual levels associated to shallow defects of QDs[23]. Therefore, the combination of these effects in the electronic structure of $Cd_{1-x}Mn_xS$ QDs (x ≠ 0) explains the nearly constant values obtained for the E_A activation energy.

In order to deduce the additional activation energies (E_B and E_C) related to other non-radiative channels of doped $Cd_{1-x}Mn_xS$ NPs (x ≠ 0), Eqs. (8) and (9) were used to fit experimental integrated PL intensities as a function of reciprocal temperature (1/T), as shown in Figs. 4b, c, and d for the concentrations x = 0.005, 0.050, and 0.100, respectively. First, E_B and E_C activation energies related to QDs were determined by using Eq. (8) in which, with exception of the previously found E_A activation energy, the following terms were used as parameters of fit: I_0^{QD} , E_B, E_C and α_n with n = A, B and C. Then, with the QD results, the activation energies related to bulk-like NCs ($E_{A'}$, and $E_{B'}$) could be found by fitting with Eq. (9).
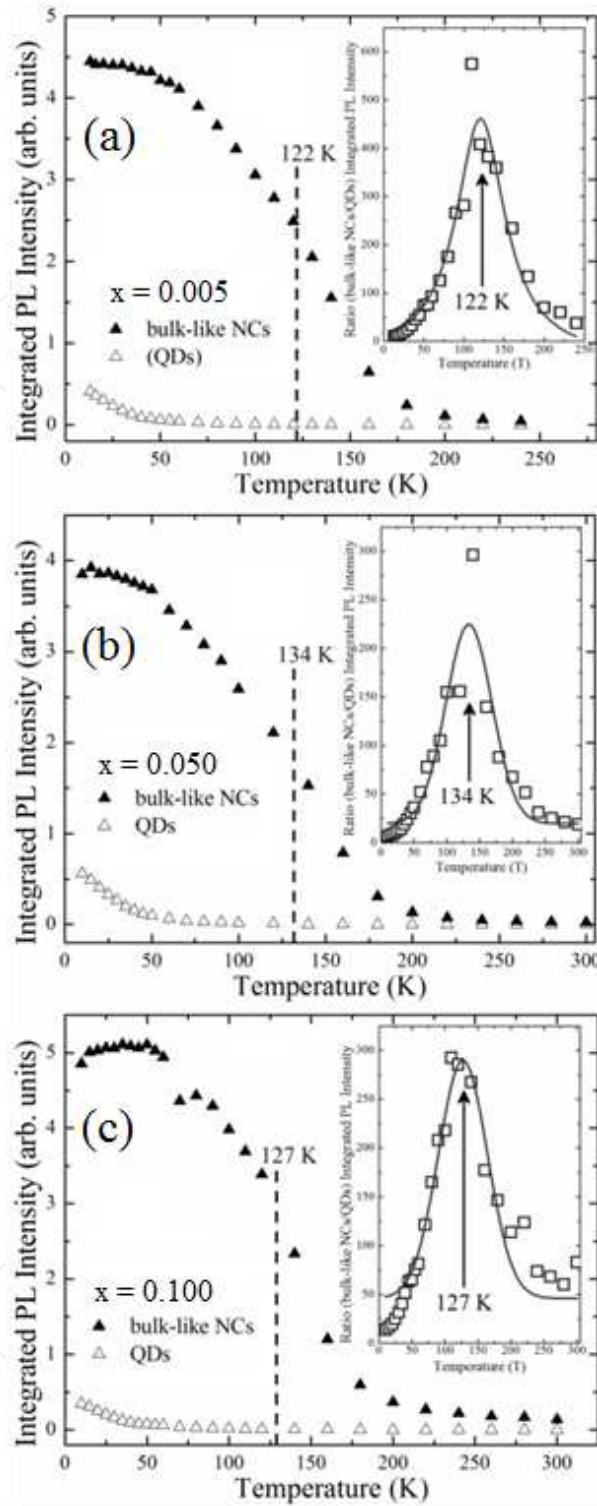
Figure 3. Temperature dependence of the integrated PL intensity of Cd$_{1-x}$Mn$_x$S NPs at several x-concentrations: (a) x = 0.005; (b) x = 0.050; and (c) x = 0.100. QDs and bulk-like NCs are represented by open and solid triangle symbols, respectively. In the inset of each panel, the square symbols represent the ratio between these integrated PL intensities (bulk-like NCs/QDs), where fitting with a Gaussian-like component was used to find the temperature corresponding to the maximum value. The dashed vertical lines show that each one of these temperatures is close to the inflection point of the integrated PL intensity of the bulk-like NCs.
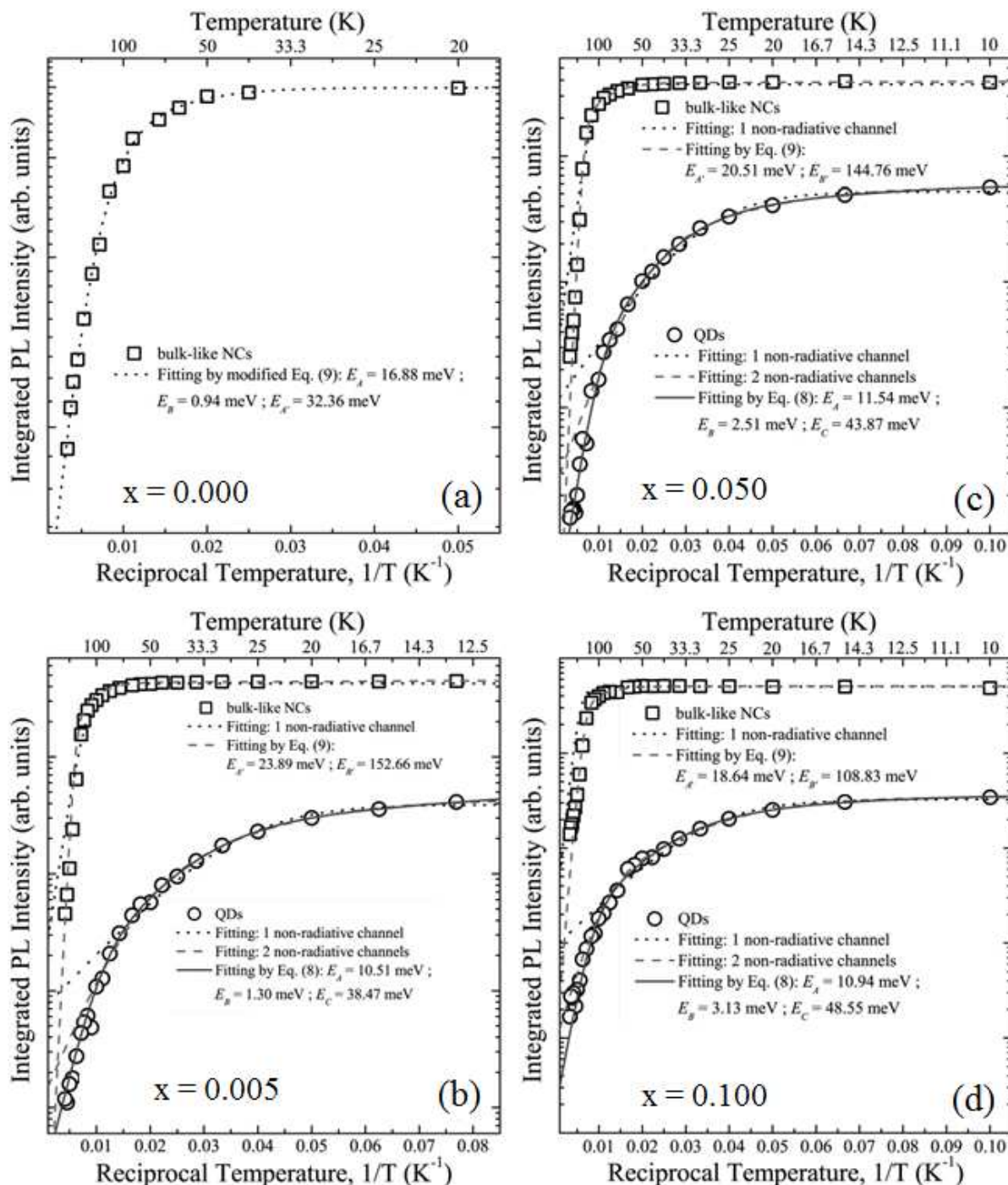
Figure 4. Experimental integrated PL intensity of Cd$_{1-x}$Mn$_x$S NPs as a function of reciprocal temperature: (a) x = 0.000; (b) x = 0.005; (c) x = 0.050; and (d) x = 0.100. Each panel shows the fitting curves for the specified equations.

For the undoped NPs (x = 0), only a PL emission band associated with the bulk-like NCs could clearly be observed (see Fig. 2a). Therefore, it was not possible to use Eq. (8) to find the activation energies associated with the QDs. In addition, since there was no magnetic doping for these NPs (x = 0), it is expected that the non-radiative channels related to Mn^{2+} ions would not exist. With these alterations, a modified Eq. (9) was used in fitting the

experimental integrated PL intensity of CdS bulk-like NCs, where the E_A, E_B, and $E_{A'}$ activation energies were considered as parameters of fit. Figure 4a shows that good fit of the experimental data was achieved which confirms the absence of non-radiative channels related to Mn^{2+} ions. Thus, even though any PL emissions from CdS QDs were not observed (see Fig. 2a), the E_A and E_B activation energies associated with them could be indirectly determined in this fitting procedure due to the carrier-mediated energy transfer from the QDs to the bulk-like NCs that is also present in the modified Eq. (9).

Furthermore, in Figs. 4b, c, and d, the fittings for both the QDs (Eq. (8)) and bulk-like NCs (Eq. (9)) are in excellent agreement with the experimental data. However, these concordances were not achieved by further fittings given: (i) one or two non-radiative channels for QDs ($x \neq 0$), and (ii) one non-radiative channel for bulk-like NCs ($x \neq 0$). Therefore, all these fittings evidently demonstrate that the Eqs. (8) and (9) for Cd$_{1-x}$Mn$_x$S NPs ($x \neq 0$), as well as the modified Eq. (9) for CdS NPs, are satisfactorily suitable for describing the temperature-dependent carrier dynamics of the $|1\rangle$ or $|1^b\rangle$ levels.

Table 1 shows all the activation energies found that are related to non-radiative channels of Cd$_{1-x}$Mn$_x$S NPs (QDs and bulk-like NCs) where, for doped NPs ($x \neq 0$), the E_A remains almost constant as previously explained. Moreover, for undoped NPs the value $E_A \sim 16.88$ meV is slightly larger than that for doped NPs ($E_A \sim 11$ meV). This proves that increases in x-concentration enhance the density of the virtual levels associated with the shallow defects of QDs. The carrier-mediated energy transfer from QDs to bulk-like NCs, a tunnelling phenomenon, is evidently being hampered due to E_B rising with increases in x-concentration (see Table I). In heavily doped NPs, there are many Mn^{2+} ions incorporated near the surface of both groups of NPs (QDs and bulk-like NCs)[22], an effect that enhances Mn–Mn interactions[17,20]. Therefore, we can conclude that high quantities of Mn^{2+} ions near the surface of these NPs weakens the coupling between their wave functions which hampers the tunnelling process from the QDs to bulk-like NCs. Consequently, this effect also contributes to the excitonic emission (E_{exc}) of Cd$_{1-x}$Mn$_x$S QDs, as observed in Fig. 2b.

x-concentration	E_A (meV)	E_B (meV)	E_C (meV)	$E_{A'}$ (meV)	$E_{B'}$ (meV)
0.000	16.88	0.94	----	32.36	----
0.005	10.51	1.30	38.47	23.89	152.66
0.050	11.54	2.51	43.87	20.51	144.76
0.100	10.94	3.13	48.55	18.64	108.83

Table 1. Behavior of activation energies (E_A, E_B, E_C, $E_{A'}$, and $E_{B'}$) related to the non-radiative channels of Cd$_{1-x}$Mn$_x$S NPs as a function of x-concentration. From the QDs, the non-radiative energy transfers are indexed as follows: (E_A) for virtual levels; (E_B) for the conduction band of the bulk-like NCs; and (E_C) for the Mn^{2+} ions. For bulk-like NCs, the non-radiative energy transfers are denoted as: ($E_{A'}$) for the virtual levels; and ($E_{B'}$) for the Mn^{2+} ions.

The non-radiative energy transfers from NPs to Mn^{2+} ions are related to the following activation energies: E_C for the QDs; and $E_{B'}$ for the bulk-like NCs. In Table I, it can be seen that E_C increases and E_B decreases with rising x-concentration. This opposite behavior between QDs and bulk-like NCs demonstrates that the **sp-d** exchange interactions are strongly dependent on the size quantum confinement of the NPs. Increasing x-concentration from 0.000 to 0.100 induces considerable blue shift in the energy gap of the QDs, which can be disregarded for the bulk-like NCs (see Fig. 1a), while the density of the $^{2,4}T$ levels of Mn^{2+} ions is being amplified. Thus, the depth of $^{2,4}T$ levels is increasing in relation to the excitonic states of QDs, while remaining almost constant for the CB of bulk-like NCs. Therefore, the combination of these effects explains very well the observed increase (decrease) in E_C ($E_{B'}$) activation energy with increasing x-concentration.

In addition, increasing x-concentration induces the density amplification of the virtual levels associated with the shallow defects of bulk-like NCs. This also occurs in the QDs[26]. However, since the change in energy gap of bulk-like NCs can be disregarded, these virtual levels become shallower for the conduction band (CB). Hence, in Table 1, the decrease in $E_{A'}$ activation energy with the increase in x-concentration can be adequately explained by taking into account this effect in the electronic structure of the bulk-like NCs.

3.2. Magneto-optical properties

Figure 5 shows the OA spectra, taken at room temperature, of $Cd_{1-x}Mn_xS$ magnetic NPs that were grown into the glass matrix environment. In Fig. 5a, the spectra were taken from NP samples with three different Mn-concentrations: x = 0.000, 0.050, and 0.100, and these samples did not have any thermal treatment. Only for comparison, the OA spectrum of the SNAB matrix is also shown in bottom of Fig. 5a and is clear the absence of any absorption band in the range between 350-650 nm. However, the OA spectra of all NP samples revealed the formation of two well defined groups of $Cd_{1-x}Mn_xS$ NPs with different sizes: (i) one group displaying a fixed band around 2.58 eV (near the energy gap of bulk CdS) and denominated as bulk-like NCs; (ii) the other displaying changing band energy due to quantum confinement properties and denominated as QDs.

A careful analysis of the bands attributed to $Cd_{1-x}Mn_xS$ QDs with concentrations x = 0.000; 0.050; and 0.100, clearly reveals a width of about 65 nm for each OA band which is due to a size distribution of the nanoparticles. From the OA peak at 3.13 eV, in Fig. 5a, and using the effective mass approximation [12,17], an average radius around R~2.0 nm was estimated for CdS QDs (x = 0.000), which confirms the strong size quantum confinement. It is noted that an increase of Mn-concentration induces a blueshift on the QDs band, from 3.13 eV, for x = 0.000, to 3.22 eV, for x = 0.100. Since these magnetic QDs were synthesized under the same thermodynamic conditions, one should expect that they have the same average dot size (R~2.0 nm) and, thus, no significant differences in their quantum confinements that would cause shift among the OA band peaks. Here, can be also inferred that the growth kinetics of these dots is not influenced by the magnetic ions, since the amount of Mn dispersed in the

glass environment is actually very small. Therefore, we attribute the blueshift on the peaks of Fig. 5a to the **sp-d** exchange interaction between electrons confined in the dot and located in the partially filled Mn^{2+} ion states. This explanation is quite reasonable[17] since the replacement of Cd by Mn, in Cd$_{1-x}$Mn$_x$S NPs, should change the energy gap between 2.58 eV, for CdS buk (x = 0) and 3.5 eV, for MnS bulk (x = 1).
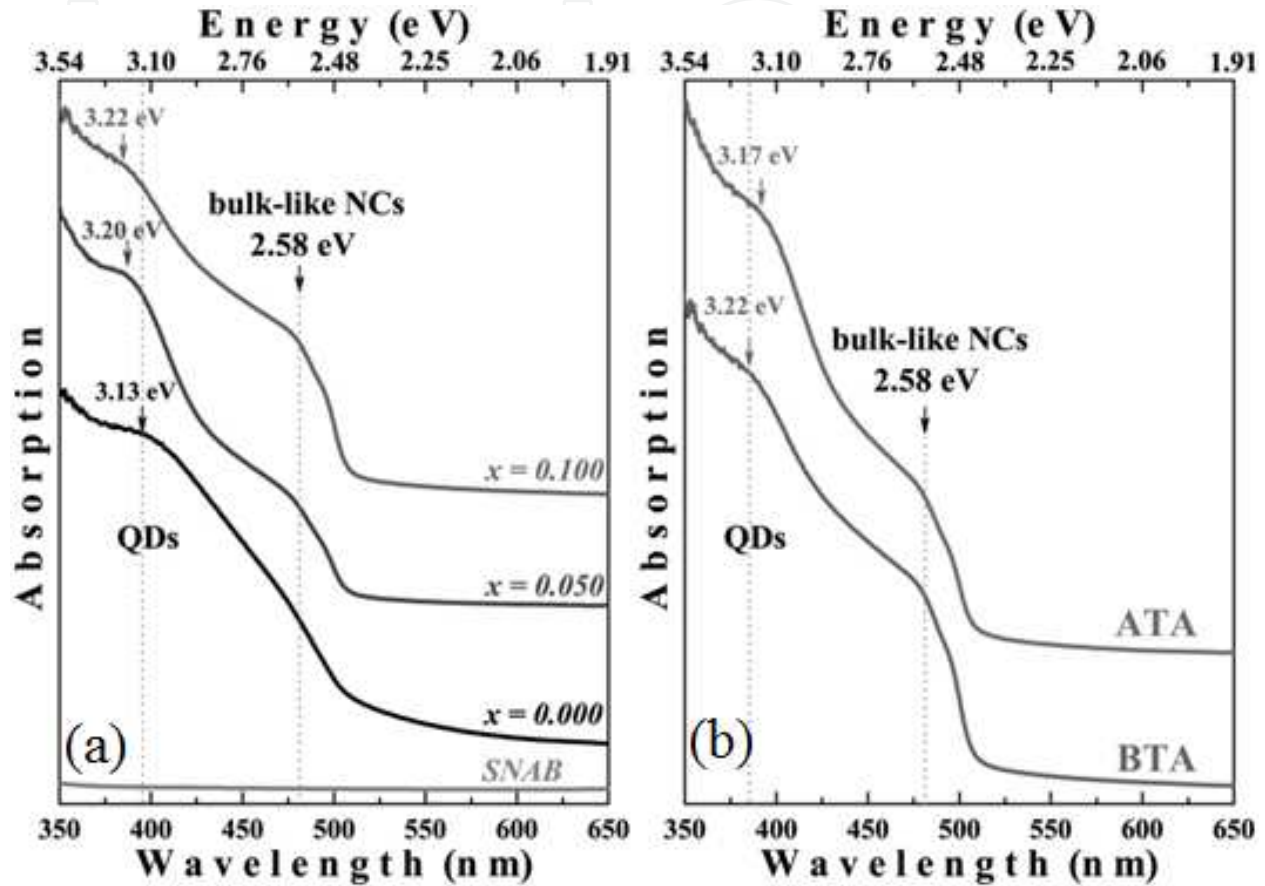

Figure 5. Room temperature OA spectra of Cd$_{1-x}$Mn$_x$S NPs embedded in the SNAB matrix. Panel (a) shows the spectra of the as-grown samples which did not receive any thermal treatment. For comparison, it is also shown the OA spectrum of the SNAB matrix, at the bottom. Panel (b) shows spectra of two identical samples containing the same magnetic ion doping (x = 0.100), but one before thermal annealing (BTA) and the other after thermal annealing (ATA) at T = 560 °C for 6 h. Observe that the peak at 2.58 eV, attributed to bulk-like NCs, does not change with doping or annealing.

We also compare the optical spectra of two identical Cd$_{0.900}$Mn$_{0.100}$S samples, one before thermal annealing (BTA) and another after thermal annealing (ATA) at 560 °C for 6h. The effect of this thermal annealing on the two OA band peaks of these NPs is shown in Fig. 5b. As expected for NPs without size quantum confinement, the OA band related to Cd$_{0.900}$Mn$_{0.100}$S buk-like NCs does not show any shift in the samples with or without thermal annealing. At the same time, the Cd$_{0.900}$Mn$_{0.100}$S QDs peak shows a redshift from 3.22 eV, in the sample without treatment (BTA), to ~3.17 eV, in the annealed sample (ATA). This shift can be ascribed to two possible annealing effects: (i) the size increase of the magnetic dot and thus, inducing weakening on the quantum confinement, and (ii) the decrease in the

effective concentration of Mn^{2+} ions incorporated into the dots during growth thus, inducing decreasing on the energy gap.

The dot size increase for increasing annealing time is a well known phenomenon governing the growth kinetic of nanoparticles in glass matrices[18,27,28]. However, a recent study of thermal treatments on undoped CdSe QDs[12] embedded in this same glass matrix (SNAB) showed a much smaller redshift (~0.03 eV) when annealed for 6 h. Since CdSe and CdS structures display great similarities, as well as $Cd_{1-x}Mn_xS$ with dilute Mn-concentration, it is reasonable to assume that they have the same growth kinetic in the same glass matrix. Thus, the higher shift (~0.05 eV) observed in $Cd_{0.900}Mn_{0.100}S$ QDs annealed for 6 h provides strong evidences that the observed higher redshift must also be ascribed to a decrease of the effective concentration of Mn^{2+} incorporated to the dots, and this decrease takes place during the thermal treatment of the sample. We shall return to this evaporation-like process later, since its understanding is still an opened subject on doping processes in semiconductor QDs[3].

Figure 6 presents the magnetic circularly polarized PL spectra, taken at 2.0 K and 15 T, of CdS (Fig. 6a) and of $Cd_{0.900}Mn_{0.100}S$ (Fig. 6b) NP samples. A decreasing from 300 K to temperatures near ~2.0 K causes an increase in the energy gap of CdS QDs, as well as in bulk CdS, of about ~ 85 meV[29]. Certainly, a similar temperature-dependent behaviour is expected for $Cd_{1-x}Mn_xS$ QDs with dot size R ~ 2 nm and for diluted magnetic doping. However, even with this large blueshift in the OA bands, the $Cd_{1-x}Mn_xS$ QDs with absorption around 405 nm, as well as all bulk-like NCs, were excited during the measurements at 2.0 K, due the large OA band width (~ 65 nm) of QDs as well as the wavelength width (± 5 nm) of the 405 nm excitation laser source. Therefore, according to OA spectra shown in Fig. 5, the emissions attributed to the two well-defined bulk-like NCs and QDs groups are observed in each spectrum of Fig. 6. The presence of virtual levels in these structures, as due to surface defects for example, can explain the asymmetric character of the emission band around 480 nm (Fig. 6b). Also, the broad emission band near 580 nm cannot be fitted by only one Gaussian-like component which provides further evidence for its complex nature associated to several emissions. We may conclude that besides the radiative recombination of excitons, labelled as E_{QD} (E_b) for the QDs (bulk-like NCs), there are also the emissions from deep defect levels, labelled as (1) and (2) for QDs and (1)$_b$ and (2)$_b$ for bulk-like NCs. These emissions detected on the PL spectra are qualitatively described in the diagram depicted in Fig. 6c where the seven emission bands are identified. The deep defect levels in CdS and $Cd_{1-x}Mn_xS$ NPs with hexagonal wurtzite structure, a common phase for these materials,[30-32] are possibly related to two energetically different divacancy defects, $V_{Cd} - V_S$, associated to the absence of Cd^{2+} and S^{2-} ions in the crystalline NP structure[20]. One divacancy is oriented along the hexagonal c-axis of the wurtzite CdS structure and assigned to trap(1), whereas the other is oriented along the basal Cd-S bond directions and assigned to trap(2)[20,21]. The size dependence of these trapping levels has been confirmed for CdSe NCs[21], and is used to explain the detected emissions from QDs (labelled E_1 and E_2) and from bulk-like NCs (labelled E_1^b and E_2^b) that occur in our $Cd_{1-x}Mn_xS$ structures, as depicted in Figs. 6.

The comparison between the emissions and absorptions of $Cd_{1-x}Mn_xS$ NPs, by taking into account the mentioned increase in energy gap at low temperature (~ 2.0 K), revels that these nanostructures embedded in a glass matrix exhibit an anomalously large Stokes shift (Δ_{SS}) given by: Δ_{SS} ~ 0.65 eV for QDs, and Δ_{SS} ~ 0.54 eV for bulk-like NCs. Possibly, the origin for this large Stokes shift can be attributed to radiative recombination due the many-body effects on the excitonic states of the NPs, a phenomenon that was recently demonstrated for PbS nanocrystals[21] and should be considered for the $Cd_{1-x}Mn_xS$ NPs. Certainly, further investigations are required in order to reach a comprehensive explanation for these observed large Stokes shifts in the $Cd_{1-x}Mn_xS$ NPs embedded in a glass matrix.

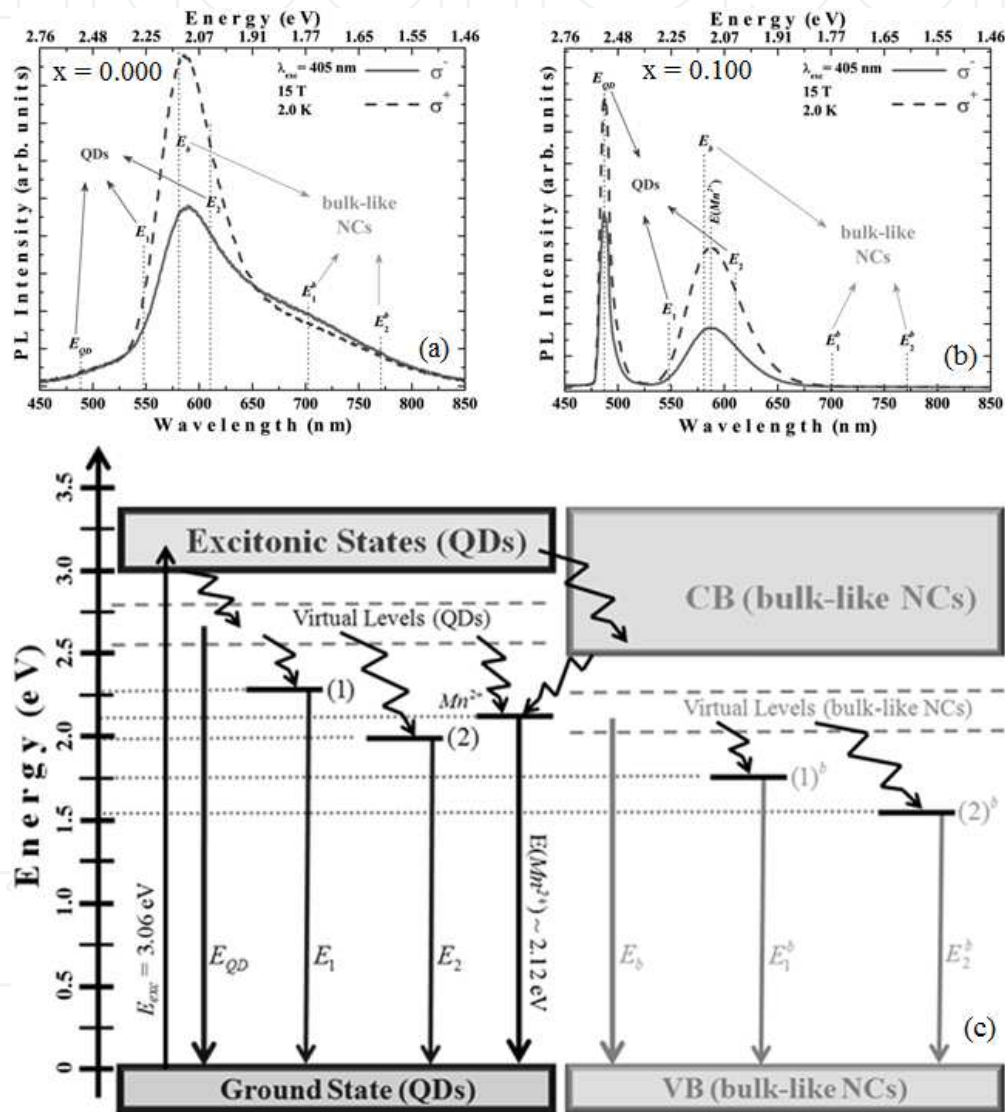**Figure 6.** Circularly polarized PL spectra, σ^- (solid lines) and σ^+ (dashed lines), taken at 2.0 K and magnetic field B = 15 T, are shown in panel (a) for undoped CdS NP sample and in panel (b) for magnetic $Cd_{0.900}Mn_{0.100}S$ NP sample. The different recombination processes are depicted in panel (c), where the emissions from QDs and from bulk-like NCs are clearly identified. The characteristic emission $E(Mn^{2+})$ of Mn^{2+} ions ($^4T_1 \rightarrow {}^6A_1$), occurring near 2.12 eV when incorporated in the II-VI semiconductors, is almost resonant with the E_b emission from bulk-like NCs. The non-radiative processes associated to the $V_{Cd} - V_S$ divacancies occurring in the structures are also indicated.

The characteristic emissions $^4T_1 \rightarrow {}^6A_1$ between levels of Mn^{2+} ions, labelled as $E(Mn^{2+})$ in Figs. 6b and 6c and with transition energy ~2.12 eV, also confirm that these magnetic impurities were substitutionally incorporated in the $Cd_{1-x}Mn_xS$ NPs[1,22,23]. This incorporation of Mn^{2+} ions in NPs has also been proved by electron paramagnetic resonance (EPR) measurements and simulations in other samples which were synthesized by the same method used in this work[17,20].

Note that the emissions from deep defect levels observed in bulk-like NCs, and shown in Figs. 6a and 6c with labels E_1^b and E_2^b, become almost suppressed in samples with magnetic doping (see Fig. 6b). Thus, Mn^{2+} ions must be filling out the Cd vacancies, V_{Cd}, during doping and this interesting fact provides further evidence not only for the existence of the deep divacancies, $V_{Cd} - V_S$, but also for the incorporation of Mn^{2+} ions in the NPs.

Figures 7a and 7b present the circularly polarized (σ^- and σ^+) PL spectra of $Cd_{0.900}Mn_{0.100}S$ NP samples without thermal treatment and taken at 2.0 K, for several magnetic field values between 0.0 and 15.0 T. The magnetic subcomponent emissions from QDs and from bulk-like NCs can be clearly observed in all PL spectra. It is also noted that σ^+ increase the intensity faster than σ^- emissions, thus resulting in the strong PL circular polarization. The relative intensity ratio between the polarized emissions from QDs and from bulk-like NCs is shown in Fig. 7c as a function of magnetic field for two different Mn-concentrations (x = 0.050 and 0.100).

The internal optical transition ($^4T_1 \rightarrow {}^6A_1$) occurring within excited $3d^5$ shells of the Mn^{2+} ions is highly sensitive to the presence of external magnetic fields[33,34]. After electron-hole pair creation by laser excitation, the band-edge exciton can either recombine radiatively or transfer its energy to a Mn^{2+} ion via an Auger-like process that depends on the exciton-Mn coupling. At low temperatures and in magnetic fields, this Mn^{2+} PL band remains unpolarized and, eventually, becomes suppressed while the circularly polarized band-edge excitonic emissions increase the intensity. This is a universal behaviour that has been observed in DMS crystals, epilayers, quantum wells, quantum wires, and in self-assembled epitaxial quantum dots[33-42]. Although the precise mechanism of energy transfer from excitons to electrons in the Mn^{2+} $3d^5$ shell is still debated in the scientific community,[37,38,42-44] the marked field dependence of this process indicates a spin-dependent excitation transfer as described by Nawrocki[45] and by Chernenko[42,43].

The energy transfer from QDs to Mn^{2+} ions is also highly sensitive to the presence of external magnetic fields[2]. For example, in self-organized $Cd_{1-x}Mn_xSe$ QD samples, the $^4T_1 \rightarrow {}^6A_1$ emissions from the incorporated Mn^{2+} ions are completely suppressed at a magnetic field values near 3–4 T [40]. According to Nawrocki model[45], this occurs because the Mn^{2+} magnetization freezes out the electron population in the $M_s = -5/2$ ground state Zeeman sublevels of the Mn^{2+} ions (labelled $^6A_1$) [2,42-45]. In this model, the transition of an electron from the conduction to the valence band occurs without change of its spin, and the transition is allowed if the total spin of the combined system of Mn-ion+electron is conserved. In particular, no Auger recombination is possible with participation of Mn-ion ground state ($^6A_1$) with spin S = 5/2 and $S_z = \pm 5/2$ since the excited state ($^4T_1$) has spin S = 3/2 and $S_z = \pm 3/2$. The suppression of the Auger recombination in the high magnetic field can be

explained by assuming thermalization of Mn-ions in the lowest state with S$_z$ = − 5/2. Thus, the band-edge excitonic emission intensity saturates with increasing magnetic field, indicating alignment of the QD exciton spins by the magnetic field.
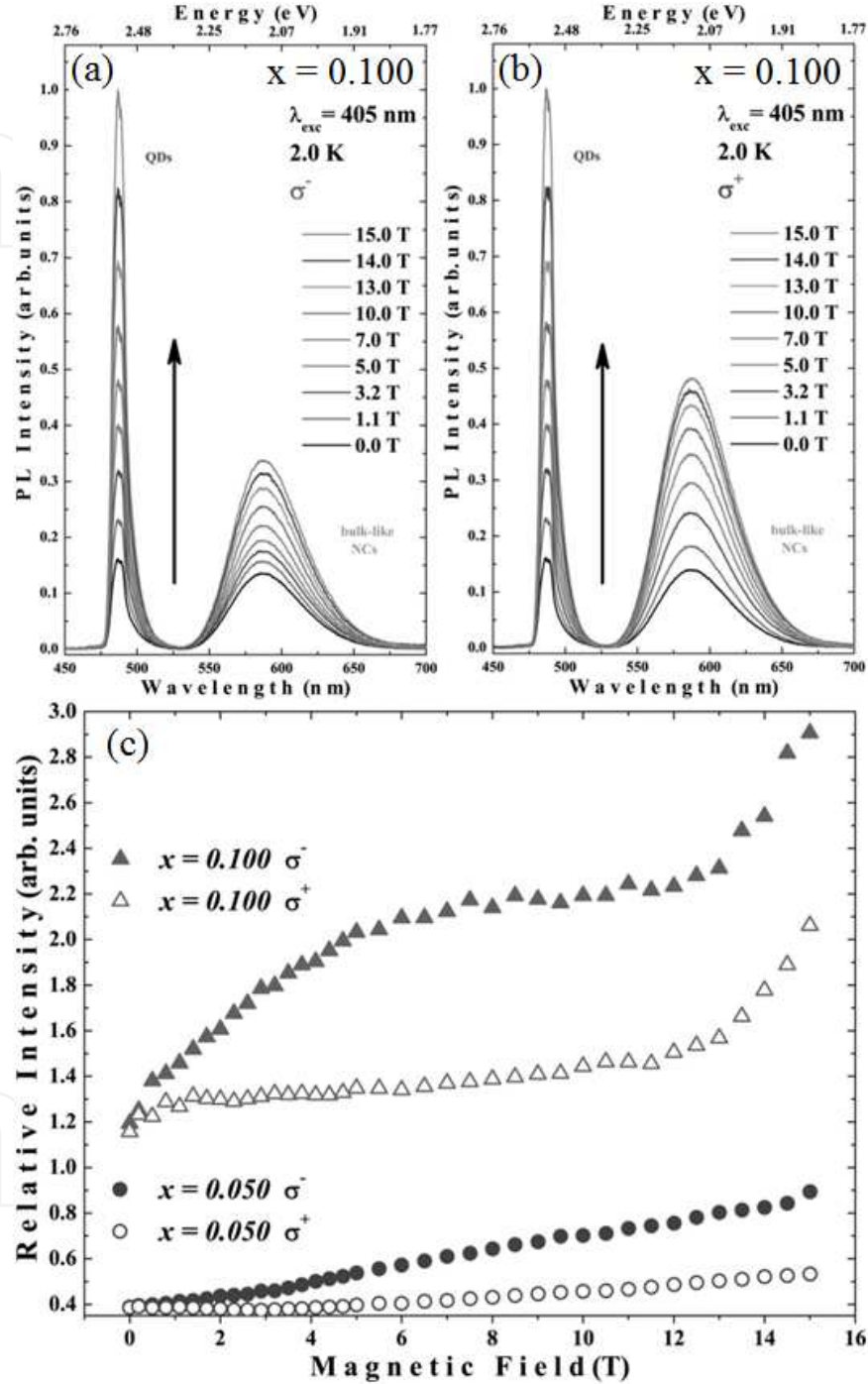

Figure 7. Circularly polarized σ⁻ (panel (a)) and σ⁺ (panel (b)) PL spectra taken at 2K for Cd$_{0.900}$Mn$_{0.100}$S NPs without thermal treatment and excited with line 405 nm of a laser source. Panel (c): Comparison between the ratio of σ⁻ (filled symbols) and σ⁺ (opened symbols) emission intensities from QDs and from bulk-like NCs in samples with concentrations x = 0.050 (circles) and x = 0.100 (triangles) for increasing magnetic field values. Notice that magnetic doping affects strongly the magnetic dependence of these intensities.

Hence, in our samples is also expected that the electron-hole radiative recombinations (E$_{QD}$ and E$_b$) show increasing intensities while the E(Mn^{2+}) emissions show decreasing change of intensities for increasing magnetic field. Because the overlap with the E$_b$ emissions in these samples, the E(Mn^{2+}) emissions cannot be clearly resolved in the PL spectra (Figs. 7a and b) but should show a change in the relative intensity (Fig. 7c). For sample with Mn-concentration x = 0.100, the ratio between polarized PL intensities from QDs and from bulk-like NCs (triangles) displays non-monotonic behaviour from 0 to 12 T with a saturation tendency, where the increased exciton emissions increase occurring at the expenses of Mn PL emissions decrease, as the magnetic fields increase. In the sample with smaller concentration, x = 0.050, the ratio between PL intensities (circles) increases almost linearly up to 15 T, or even with slight intensity change. In Fig. 7c, it is also noted a significant change in the relative intensities of emissions for σ$^-$ polarization, starting at B ~ 4 T, in the sample with higher Mn-concentration (x = 0.100) and a much lower intensity change in the sample with Mn-concentration x = 0.050. It is our understanding that this effect is related to the suppressed E(Mn^{2+}) emissions.

Furthermore, in Fig. 7c, the x-concentration dependent behaviour of the exciton intensity variation with the magnetic field indicates a strong modification of the Auger energy transfer rate from the excitons to Mn^{2+} ions. Therefore, in the low Mn-concentration this energy transfer does not occur as strongly as in the case of the high Mn-concentration. It has been shown that Auger energy transfer is sensitively dependent on carrier density – excitation power[40,42] and Mn-concentration [36]. In the high power excitation, the suppression of the Auger process does not take place as strongly as in the case of the weak power excitation even in the high magnetic field region. In the low excitation intensity the PL intensity curve behaves very different as in the high excitation intensity. Based on the approach of Nawrocki et al.[45], Chernenko et al.[42,43] calculated the increase in the exciton intensity with B and showed that this increasing is associated with lifetime of non-radiative transition $I(B)/I(0) = const/\left(1+\left(\tau_0/\tau_A\right)\right)$ were τ_0 and τ_A are the times of radiative and non-radiative recombinations of the exciton, respectively. Here, the effective time of non-radiative recombination depends on B, Mn-concentration and carrier density [36,42-44]. Similar behaviour of the dependence of the PL intensity with B is observed for our samples with different Mn-concentrations. Note that the emissions from deep defect levels observed in bulk-like NCs, and shown in Figs. 6a and 6c with labels E_1^b and E_2^b, become almost suppressed in samples with magnetic doping (see Fig. 6b). Thus, Mn^{2+} ions must be filling out the Cd vacancies, V$_{Cd}$, during doping and this interesting fact provides evidence that Mn^{2+} doping can alter the carrier density in the NPs.

The Zeeman energy splitting in the electronic structure of the NPs is also other important effect caused by the increasing in the magnetic field. It is well known that in DMS structures the Zeeman energy splitting can be considerably altered by the exchange interaction between the carrier spins and the substitutional doping magnetic ions[46]. Thus, in our Cd$_{1-x}$Mn$_x$S NP samples, it is quite expected different Zeeman energy splitting for QDs and bulk-like NCs with the increase in the magnetic field. This in turn should also increase the

separation between the excited electronic levels of QDs and bulk-like NCs, so that the non-radiative energy transfer between them (as depicted in Fig. 6b) is being weakened up to be completely interrupted at a given magnetic field value. We understand that this phenomenon occurs at a magnetic field B ~ 12 T for the Cd$_{1-x}$Mn$_x$S NP sample with x = 0.100, contributing thus to the abrupt increase in relative PL intensity (QDs/bulk-like NCs) shown in Fig. 7c. Since this effect cannot be clearly observed for the Cd$_{1-x}$Mn$_x$S NP samples with x = 0.050, we can conclude that non-radiative energy transfer involving the excited electronic levels of QDs and bulk-like NCs was not completely broken off in the investigated magnetic field range, favouring the almost linear behaviour observed in Fig. 7c. It is important to mention that the energy transfers involving the excitonic states of QDs, the conduction band of bulk-like NCs, and the shallow virtual levels of NPs was demonstrated in section 3.1 (carrier dynamics)[47].
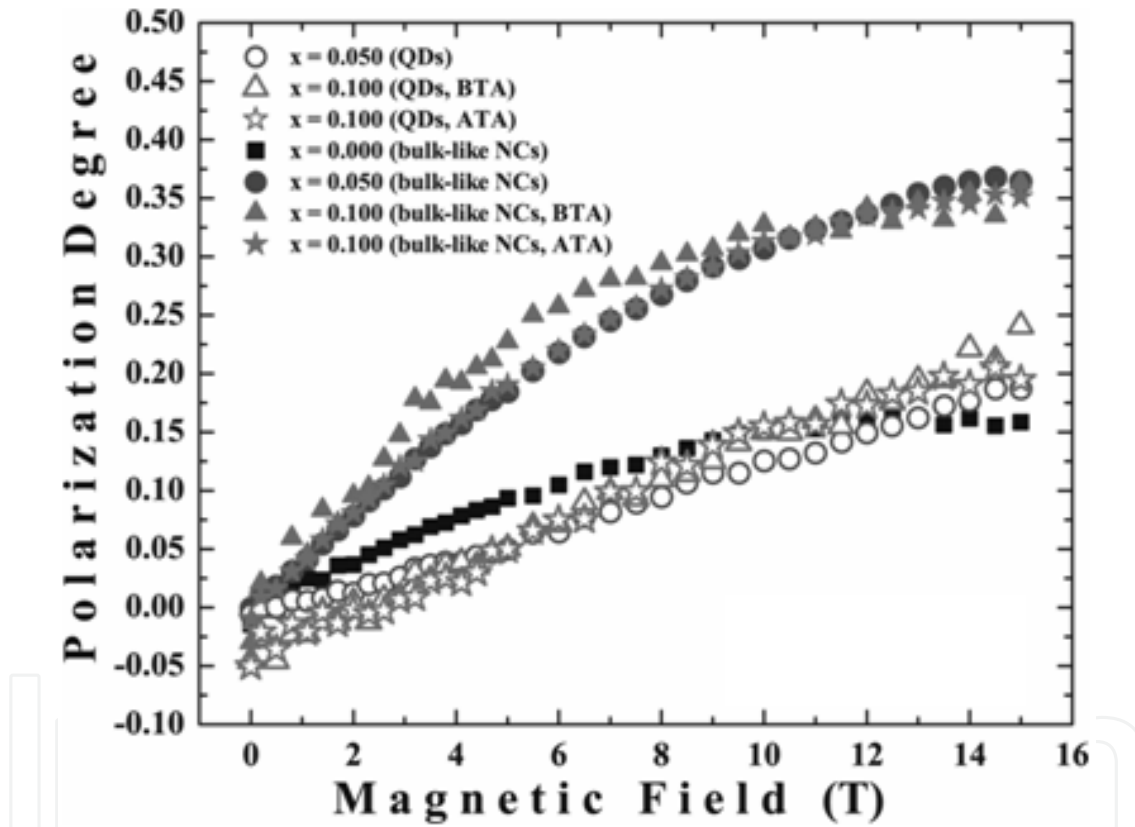

Figure 8. Magnetic field dependence of the polarization degree ($\rho(B)$) of Cd$_{1-x}$Mn$_x$S NPs: QDs (open symbols) and bulk-like NCs (filled symbols). For a comparison it is shown the degrees of polarization for two identical samples with concentrations x = 0.100, but one before thermal annealing (BTA) and another after undergoing thermal annealing (ATA) at T = 560 ºC for 6 h.

The degree of polarization is defined by $\rho(B) = (I_+ - I_-)/(I_+ + I_-)$ **[2,41,46],** where I_+ and I_- are the integrated intensities of σ^+ and σ^- magnetic circularly polarized PL (MCPL) spectra taken at a given magnetic field, B. The values of $\rho(B)$ for bulk-like NCs and for QD emissions are represented by filled and opened symbols in Fig. 8, respectively. For QD emissions, $\rho(B)$ increases almost linearly up to B = 15 T, and reaches 25% polarization. The

bulk-like NC emissions appear to increase quadratically with B and, at higher magnetic fields, show a saturation tendency near 35%. However, the degree of polarization for CdS bulk-like NCs (x = 0.000) shows a much slower increase with saturation value near 15%. In the Mn-doped samples (x ≠ 0), the bulk-like NCs exhibit a higher degree of polarization than the QDs, thus evidencing that the amount of Mn^{2+} ions that are substitutionally incorporated into QDs is smaller than in the bulk-like NC. Evidently, this effect is related to the well known difficulty in doping semiconductor QDs with magnetic impurities. Furthermore, the mentioned non-radiative energy transfer from QDs to bulk-like NCs is also a cause for the lower degree of polarization for the QDs. It is fascinating to note that the degree of polarization for the $Cd_{1-x}Mn_xS$ QDs with x = 0.100 becomes higher than for the undoped bulk-like NCs (x = 0) at the same magnetic field in which the abrupt increase in relative PL intensity (Fig. 7c) takes place, i. e., B ~ 12 T. For the $Cd_{1-x}Mn_xS$ QDs with x = 0.050 this effect is less pronounced and occurs at a higher magnetic field (see Fig. 8). In addition, the different magneto-optical properties of the bulk-like NCs and QDs can be explained by taking into account a considerable change of exchange interaction between the carrier spins and the substitutional doping of magnetic ions incorporated into the NPs with different sizes. This fact confirms that the size quantum confinement plays important role on the magneto-optical properties of $Cd_{1-x}Mn_xS$ NPs. We note that the Mn-doped with x = 0.050 and undoped CdS NP samples does not exhibit any zero-field degree of polarization. However, the samples doped with x = 0.100 presented negative zero-field polarization, $\rho(B=0) \cong -5\%$, which is ascribed to a change in the Zeeman ground state character. This interesting phenomenon is related to an intrinsic magnetism of $Cd_{1-x}Mn_xS$ NPs caused by the change in the **sp-d** exchange interaction strength, which is strongly dependent on the doping mole fraction x of incorporated magnetic ions.

A comparison between the degrees of polarization for two sets of identical Mn-doped samples with x = 0.100, is shown in Fig. 8, one before thermal annealing, labelled BTA and represented by triangles symbols; another undergone a thermal annealing at T = 560 ºC for 6 h, labelled ATA and represented by star symbols. After thermal annealing, the $Cd_{0.900}Mn_{0.100}S$ bulk-like NCs sample showed a degree of polarization very similar to the $Cd_{0.950}Mn_{0.050}S$ bulk-like NCs sample. This fact indicates that during the thermal annealing at T = 560 ºC occurred a decrease in the effective concentration (x_{eff}) of the $Cd_{1-x}Mn_xS$ bulk-like NCs. In agreement with observed redshift for OA band shown in Fig. 5b, this same dynamical doping process should also occur in the $Cd_{1-x}Mn_xS$ QDs. However, as shown in Fig. 8 (see open triangle and star symbols), the change in degree of polarization for QDs induced by thermal annealing is small due to two effects: (i) the strong localization of magnetic Mn^{2+} ions in the same place as the charged carries confined to the dots, and (ii) the mentioned smaller amount of magnetic impurity that is incorporated into QDs.

Figures 9 (a, b, and c) presents two-dimensional phase MFM images (room temperature) of the $Cd_{1-x}Mn_xS$ NPs (x = 0.100) that are located at the samples surface, where it is possible to investigate the thermal annealing effect on the total magnetic moment of NPs. The images (150 x 150 nm) with a lift of 20 nm were recorded in two situations: in Fig. 9a before thermal

annealing (BTA); and in Fig. 9c after thermal annealing (ATA). The contrast between these MFM images is a result of the interactions between the tip and the NP magnetization. However, there is also a small influence of the sample topography because the probe is close to the sample surface (20 nm). As a result of magnetic interaction between tip and surface, the bright area (dark area) of the phase MFM image displays repulsive (attractive) interaction. Thus, the clear contrast that is observed in Fig. 9a, which is mainly caused by magnetic interactions with the NPs, is almost vanished after thermal annealing as shown in Fig. 5c. Hence, we may conclude that the total magnetic moment of each NP (observed in Fig. 9a) is caused by the **sp-d** exchange interactions and can be tuned by a suitable thermal annealing of the Cd$_{1-x}$Mn$_x$S NP samples. In agreement with the results of Figs. 5 and 8, this behaviour can ascribed to diffusion of Mn^{2+} ions from the core to a position near the NP surface and, therefore, decreasing the effective concentration (x$_{eff}$) in Cd$_{1-x}$Mn$_x$S samples. In addition, Figure 9b shows the phase MFM image (30 x 30 nm) obtained with no lift, of a Cd$_{1-x}$Mn$_x$S NP (BTA) that is at the sample surface. Since this image was recorded with no lift, there is a strong influence of the sample topography and allowing the observation of the characteristic hexagon of the wurtzite structure.
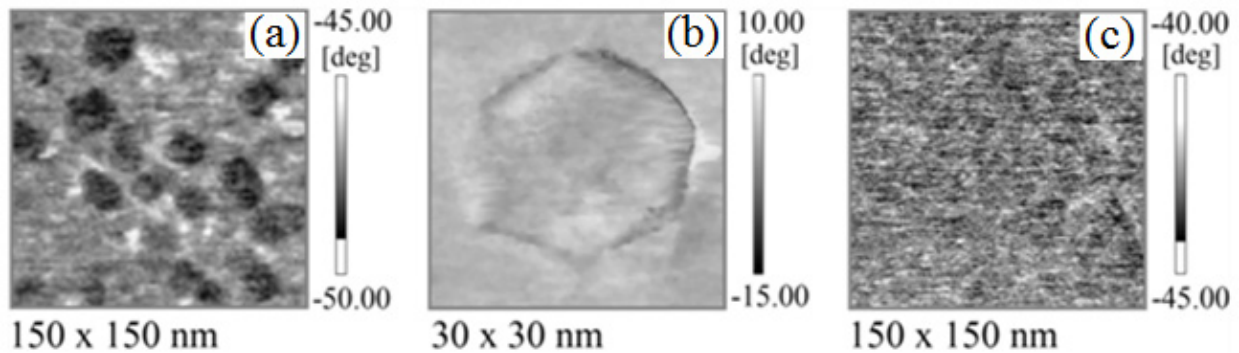

Figure 9. Room temperature phase MFM images (150 x 150 nm) with a lift of 20 nm of two Cd$_{0.900}$Mn$_{0.100}$S samples: (a) before thermal annealing (BTA); and (C) after thermal annealing (ATA). Panel (B): Phase MFM image (30 x 30 nm) with no lift of a NP before thermal annealing, where the characteristic hexagon of the wurtzite structure can be observed.

The main doping models for QDs that are used to explain the incorporation of impurities, including Mn^{2+} as in our samples, are known as 'trapped-dopant' and 'self-purification' mechanisms, which have being largely discussed in last few years[3,48-52]. The trapped-dopant mechanism is governed by the growth kinetics, where the impurity is adsorbed on the dot surface and then covered by additional material,[3] while the self-purification mechanism is governed by a diffusion process of impurities to more stable and stronger binding energy sites near the surface of dots[48].

It becomes clear that the trapped-dopant mechanism is occurring in the course of the thermal annealing at T = 560 ºC of our sample, since the $Cd_{1-x}Mn_xS$ QDs are growing due to increasing annealing time (see Fig. 5b). However, it is necessary to answer the question: Is this mechanism responsible for the decreasing x-concentration of Mn^{2+} ions in the QDs? In our conception, it is reasonable to assume that the trapped-dopant mechanism does not account for a significant change of Mn-concentration during the $Cd_{1-x}Mn_xS$ dot growth by the melting-nucleation synthesis. Since there is a relative homogeneous distribution of Cd^{2+}, Mn^{2+} and S^{2-} species into the glass environment in each moment of the thermal annealing, it is expected to observe nearly constant Mn-concentration in the $Cd_{1-x}Mn_xS$ dot growth process. Furthermore, the trapped-dopant mechanism is generally dominant for QD synthesis based on liquid phase approach, as the colloidal chemistry, where the temperatures are generally below 350 ºC and, in some case, even as low as room temperature[3,53]. In contrast, the energetic argument related to the self-purification mechanism imposes a relative instability for the impurity species due to increasing formation energy for decreasing dot-size. In Mn-doped CdSe NCs, for example, it is known that the diffusion of Mn^{2+} ions occurs at a synthesis temperature around ~550 K (277 ºC), due to this instability [54,55]. Therefore, we are convinced that the relatively high temperature used in thermal annealing of our sample (560 ºC) is able to provide enough energy to provoke impurity diffusion toward surface region, a site having stronger binding energy, or even to evaporate the magnetic impurity ions from the $Cd_{1-x}Mn_xS$ QDs. In other words, our results confirm that self-purification is the dominant mechanism that controls the doping in semiconductor QDs grown by melting-nucleation synthesis approach.

4. Conclusions

In conclusion, we have recorded optical absorption (OA), photoluminescence (PL), and magnetic circularly polarized photoluminescence (MCPL) spectra, as well as magnetic force microscopy (MFM) images, in order to investigate $Cd_{1-x}Mn_xS$ NPs that were synthesized in a glass matrix. Room temperature OA spectra revealed the growth of two groups of NPs with different sizes: QDs and bulk-like NCs, a result confirmed by MFM images. Several emissions were observed in the temperature dependent PL spectra of $Cd_{1-x}Mn_xS$ NPs, including those from deep defect levels that were attributed to two energetically different divacancies, V_{Cd}–V_S, in the wurtzite structure. Moreover, the emissions from these deep defect levels were suppressed with increasing x-concentration, providing further evidence not only of the incorporation of Mn^{2+} ions in the NPs, but also for the existence of deep divacancy defects V_{Cd} – V_S. Therefore, we have demonstrated that the density of NP defects can be controlled by magnetic doping. From the temperature dependent PL spectra of these NPs, we have deduced, based on rate equation, expressions in order to describe the carrier dynamics between excitonic states of QDs and conduction band of bulk-like NCs. Fitting procedures with these coupled expressions achieved satisfactory agreement with the integrated PL intensity of both the QDs and bulk-like NCs provided activation energies of non-radiative channels observed in $Cd_{1-x}Mn_xS$ NPs.

Our results confirm that the magnetic doping, Mn^{2+} ions localization, and quantum confinement play important roles on the magneto-optical properties of these NPs. The different behaviour observed between the two groups of NPs with different sizes, QDs and bulk-like NCs, were ascribed to a considerable change of exchange interaction between the carrier spins and the substitutional doping magnetic ions incorporated into the NPs. In addition, we have demonstrated that the relatively high temperature that was used in the thermal annealing of the samples provides enough energy to provoke magnetic impurity diffusion toward surface region of NPs. Therefore, for semiconductor QDs grown by the melting-nucleation synthesis approach, the doping process is dominated by the self-purification mechanism. We believe that the main results of this chapter can motivate further investigations and applications of other systems containing DMS NPs.

Author details

Noelio Oliveira Dantas and Ernesto Soares de Freitas Neto
Laboratório de Novos Materiais Isolantes e Semicondutores (LNMIS), Instituto de Física,
Universidade Federal de Uberlândia,Uberlândia, Minas Gerais, Brazil

Acknowledgement

5. References

[1] Archer P I, Santangelo S A, Gamelin D R (2007). Nano Lett. 7: 1037.

[2] Beaulac R, Archer P I, Ochsenbein S T, Gamelin D R (2008). Adv.Funct.Mater. 18: 3873.

[3] Norris D J, Efros A L, Erwin S C (2008).Science. 319: 1776.

[4] Gur I, Fromer N A, Geier M L, Alivisatos A P (2005).Science. 310: 462.

[5] Erwin S C, Zu L , Haftel M L, Efros A L, Kennedy T A, Norris D J (2005). Nature. 436: 91.

[6] Yu J H, Liu X, Kweon K E, Joo J, Park J, Ko K –T, Lee D W,Shen S, Tivakornsasithorn K, Son J S, Park J –H, Kim Y –W, Hwang G S, Dobrowolska M, Furdyna J K, Hyeon T (2010).Nature Materials. 9: 47.

[7] Beaulac R, Archer P I, Liu X, Lee S, Salley G M, Dobrowolska M, Furdyna J K, Gamelin D R (2008).Nano Lett. 8: 1197.

[8] Bacher G, Schweizer H, Kovac J, Forchel A, Nickel H, Schlapp W, Lösch R (1991). Phys Rev B. 43: 9312.

[9] Felici M, Polimeni A, Miriametro A, Capizzi M, Xin H P, Tu C W (2005). Phys Rev B. 71:045209.

[10] Sanguinetti S, Henini M, Alessi M Grassi, Capizzi M, Frigeri P, Franchi S (1999). Phys Ver B. 60: 8276.

[11] Banyai L, Koch S W (1993) Semiconductor Quantum Dots. Singapore: World Scientific Publishing Co.

[12] Freitas Neto E S, Dantas N O, da Silva S W, Morais P C, Pereira-da-Silva M A (2010). J Raman Spectrosc. 41: 1302.

[13] Beaulac R, Archer P I, Ochsenbein S T, Gamelin D R (2008). Adv Funct Mater. 18: 3873.

[14] Mocatta D, Cohen G, Schattner J, Millo O, Rabani E, Banin U (2011). Science. 332: 77.

[15] Brus L E (1984).J Chem Phys. 80: 4403.

[16] Grahn H T (1999) Introduction to Semiconductor Physics, World Scientific Publishing Co. Pte. Ltd., New York. Ch 9.

[17] Dantas N O, F Neto E S, Silva R S, Jesus D R, Pelegrine F (2008). Appl Phys Lett. 93:193115.

[18] Freitas Neto E S, da Silva S W, Morais P C, Vasilevskiy M I, Pereira-da-Silva M A, Dantas N O (2011). J Raman Spectrosc. 42: 1660.

[19] Harrison M T, Kershaw S V, Burt M G, Rogach A L, Kornowski A, Eychmüller A, Weller H (2000). Pure Appl Chem. 72: 295.

[20] Freitas Neto E S, Dantas N O, Barbosa Neto N M, Guedes I, Chen F (2011). Nanotechnology. 22: 105709.

[21] Babentsov V, Riegler J, Schneider J, Ehlert O, Nann T, Fiederle M (2005). J Cryst Growth. 280: 502.

[22] Zhou H, Hofmann D M, Alves H R, Meyer B K (2006). J Appl Phys. 99:103502.

[23] Beaulac R, Archer P I, Van Rijssel J, Meijerink A, Gamelin D R (2008).Nano Lett. 8: 2949.

[24] Lourenço S A, Silva R S, Andrade A A, Dantas N O (2010). J Lumin. 130: 2118.

[25] Lourenço S A, Dias I F L, Poças L C, Duarte J L, de Oliveira J B B, Harmand J C (2003). J Appl Phys. 93: 4475.

[26] Tripathi B, Singh F, Avasthi D K, Das D, Vijay Y K (2007). Physica B (Amsterdam). 400: 70.

[27] Dantas N O, Silva R S, Pelegrini F, Marques G E (2009). Appl Phys Lett. 94: 26310.

[28] Dantas N O, Freitas Neto E S, Silva R S (2010) Diluted Magnetic Semiconductor Nanocrystals in Glass Matrix, Misc: in Nanocrystals (ed. Y. Masuda). Rijeka: InTech. 143 p. Book Chapter

[29] Vossmeyer T, Katsikas L, Giersig M, Popovic I G, Diesner K, Chemsiddine A, Eychmüller A, Weller H (1994). J Phys Chem. 98: 7665.

[30] Jain M K (1991). Diluted Magnetic Semiconductor (ed. M.K.Jain).World Scientific Publishing Co., Singapore. Ch.1, 12 p. Book Chapter.

[31] Cheng Y, Wang Y, Bao F, Chen D (2006). J Phys Chem B. 110: 9448.

[32] Xue H T, Zhao P Q (2009). J Phys D: Appl Phys. 42:015402.

[33] Furdyna J K (1988). J Appl Phys. 64: R29.

[34] Becker W M (1988) Semiconductors and Semimetals, in Diluted Magnetic Semiconductors (ed. J. K. Furdyna and J. Kossut) Academic Press, San Diego,vol. 25; Dietl T (1994), in Handbook on Semiconductors (ed. T. S. Moss and S. Mahajan), North-Holland, Amsterdam.

[35] Lee Y R, Ramdas A K, Aggarwal R L (1988).Phys. Rev. B: Condens. Matter. 38: 10600.

[36] Kim C S, Kim M, Lee S, Kossut J, Furdyna J K, Dobrowolska M (2000). J Cryst Growth. 214–215: 395.

[37] Lee S, Dobrowolska M, Furdyna J K (2005). Phys Rev B: Condens Matter. 72: 075320.

[38] Falk H, Hübner J, Klar P J, Heimbrodt W (2003). Phys. Rev. B: Condens. Matter. 68: 165203; Agekyan V F, Holtz P O, Karczewski G, Moskalenko E S, Yu A (2010). Serov and N. G. Filosofov. Phys Solid State. 52: 27.

[39] Cooley B J, Clark T E, Liu B Z, Eichfeld C M, Dickey E C, Mohney S E, Crooker S A, Samarth N (2009). Nano Lett. 9 : 3142.

[40] Oka Y, Kayanuma K, Shirotori S, Murayama A, Soum I, Chen Z (2002). J Lumin. 100: 175.

[41] Hundt A, Puls J, Henneberger F (2004). Phys Rev B: Condens Matter. 69: 121309(R).

[42] Chernenko A V, Dorozhkin P S, Kulakovskii V D, Brichkin A S, Ivanov S V, Toropov A A (2005). Phys Rev B: Condens Matter. 72: 045302.

[43] Chernenko A V, Brichkin A S, Sobolev N A, Carmo M C (2010). J Phys : Condens Matter. 22: 355306.

[44] Viswanatha R, Pietryga J M, Klimov V I, Crooker S A (2011). Phys Rev Lett. 107: 067402.

[45] Nawrocki M, Rubo Yu G, Lascaray J P, Coquillat D (1995). Phys Rev B: Condens Matter. 52: R2241.

[46] Schmidt T, Scheibner M, Worschech L, Forchel A, Slobodskyy T, Molenkamp L W (2006). J Appl Phys. 100: 123109.

[47] Freitas Neto E S, Dantas N O, Lourenço S A (2012). Phys Chem Chem Phys. 14: 1493.

[48] Dalpian G M, Chelikowsky J R (2006). Phys Rev Lett. 96: 226802.

[49] Du M.-H, Erwin S C, Efros A L, Norris D J (2008). Phys Rev Lett. 100: 179702.

[50] Dalpian G M , Chelikowsky J R (2008). Phys Rev Lett. 100: 179703.

[51] Chan T.-L, Tiago M L, Kaxiras E, Chelikowsky J R (2008). Nano Lett. 8: 596.

[52] Erwin S C (2010). Phys Rev B: Condens Matter. 8: 235433.

[53] Chan T.-L, Kwak H, Eom J.-H, Zhang S B, Chelikowsky J R (2010). Phys Rev B: Condens Matter. 82: 115421.

[54] Chan T.-L, Zayak A T, Dalpian G M, Chelikowsky J R (2009). Phys Rev Lett. 102: 025901.

[55] Rosenthal S J, McBride J, Pennycook S J, Feldman L C (2007).Surf Sci Rep. 62: 111.